nanomaterials

MDPI

Article

Heterostructure Composites of CoS Nanoparticles Decorated on $Ti_3C_2T_x$ Nanosheets and Their Enhanced Electromagnetic Wave Absorption Performance

Hui Liu [1], Ling Li [2,*], Guangzhen Cui [1,*], Xinxin Wang [1], Zhi Zhang [1] and Xuliang Lv [2]

[1] Graduate School, The Army Engineering University of PLA, Nanjing 210007, China; liuhh1005@163.com (H.L.); 18260093995@163.com (X.W.); zhangnjjn@163.com (Z.Z.)

[2] Engineering College of Field Engineering, The Army Engineering University of PLA, Nanjing 210007, China; xllu1957@126.com

* Correspondence: leonleeust@hotmail.com (L.L.); cgzovezy@163.com (G.C.)

Received: 10 July 2020; Accepted: 20 August 2020; Published: 26 August 2020

Abstract: As a typical two-dimensional material, MXene possesses excellent conductivity and tunable interlayer space, which makes it have an impressive development potential in the field of electromagnetic (EM) waves absorbing materials. In this work, we fabricated a sandwich structure CoS@$Ti_3C_2T_x$ composite using a simple solvothermal process. The CoS nanoparticles are anchored on the $Ti_3C_2T_x$ MXene sheets, forming a heterolayered structure. The results demonstrate that the CoS@$Ti_3C_2T_x$ composites with the sandwich-like architecture showed excellent EM absorbing performance due to the synergistic effects of the conductivity loss, interface polarization, and dipole polarization. When the doping ratio was 40 wt %, the maximum reflection loss value of CoS@$Ti_3C_2T_x$ was up to –59.2 dB at 14.6 GHz, and the corresponding effective absorption bandwidth (below –10 dB) reached 5.0 GHz when the thickness was only 2.0 mm. This work endows a new candidate for the design of MXene-based absorption materials with optimal performance.

Keywords: MXene $Ti_3C_2T_x$; CoS nanoparticle; dielectric loss; microwave absorption

1. Introduction

Electromagnetic (EM) pollution has emerged from the explosive development of military equipment, and communication technology has produced serious damage for human beings [1,2]. Thus, microwave absorption materials have attracted increasing attention, which effectively converts the EM energies into thermal energies [3,4]. Strong EM wave attenuation intensity and wide effective bandwidth are the pursuits for the preparation of superior absorbing materials [5]. Meanwhile, light weight and high efficiency are also two key factors affecting their wide application in daily life [6,7]. To date, a great number of absorbing materials have been reported such as carbon materials (nanoporous carbons, graphene, CNTs, carbon fibers), conductive polymers (PPy, PANI), and semiconductor transition-metal sulfides (CuS, MoS_2), etc. Mohd Najim et al. used nickel–phosphorus coating on the tetrapod-shaped ZnO by the electroless coating process. The Ni–P coating increased the magnetic loss of the material, and the maximum reflection loss (RL) of the Ni–P coated T–ZnO reached –36.41 dB with an effective absorption bandwidth of 10.0 GHz [8]. Wang et al. designed a $CoFe_2O_4$/N-RGO aerogel wherein $CoFe_2O_4$ was embedded in the N-doped reduced graphene oxide (RGO) aerogels and the strongest RL was –60.4 dB at 14.4 GHz [9].

Notably, MXene, a typical 2D structure composed of transition-metal carbides, nitrides, and/or carbonitrides, has gained interest in the field of EM wave absorbing [10]. Due to their special laminated

structure, high conductivity, and huge specific surface area, MXene exhibits huge potential application in lithium-ion batteries [11], supercapacitors [12], EM interference shielding [13], and EM wave absorbers [14]. As we all know, $Ti_3C_2T_x$, where T_x represents the surface terminations (such as –OH, =O, –F) after etching by hydrofluoric acid, is the first MXene material discovered by Yury Gogotsi [15–17]. These surface functional groups will induce extra dipoles to generate dipole polarization, which may enhance the dielectric loss and optimize impedance matching [18]. Nevertheless, the impedance matching of sole MXene is poor due to the high conductivity, which cannot meet the absorption requirements of strong absorption, broad bandwidth, light-weight, and thin thickness. For instance, Zhang et al. fabricated $Ti_3C_2T_x$ MXene materials; when the filler loading was up to 50 wt %, the maximum RL of $Ti_3C_2T_x$ MXene was –29.6 dB with a thickness of 1.8 mm and the effective absorption bandwidth was less than 3 GHz [19]. Previous studies have confirmed the principle that the combination of MXene and other materials can effectively construct the heterogeneous, which is beneficial to attenuate the EM energies such as $Ti_3C_2T_x$@RGO [20], $Ti_3C_2T_x$@Ni [21], $Ti_3C_2T_x$/CNTs [22], and $Ti_3C_2T_x$@poly (vinyl alcohol) [23]. Among them, the composite of $Ti_3C_2T_x$ and nanomaterials has been found to further improve the absorption performance. Liu et al. prepared $TiO_2/Ti_3C_2T_x/Fe_3O_4$ composites by the hydrothermal process [24]. The ultrasmall sized Fe_3O_4 introduces an abundant surface area, which increases the multiple scattering and reflection between the $Ti_3C_2T_x$ interlayers. The maximum RL was –57.3 dB (at 10.1 GHz) and the corresponding thickness was 1.9 mm. However, the effective absorption bandwidth of the $TiO_2/Ti_3C_2T_x/Fe_3O_4$ composites was only 2.1 GHz (6.6–8.7 GHz) while the doping ratio of powder in paraffin was up to 70 wt %, indicating that further optimization is needed in the terms of the absorption bandwidth and weight. Cui et al. reported that the two-dimensional (2D) $Ti_3C_2T_x$ modified with CuS nanoparticles exhibited a minimum RL value of –43.5 dB at 2.0 mm, in which the effective absorption bandwidth was up to 5.2 GHz [25]. It was confirmed that MXene can be combined with transition metal sulfide for application in absorbing materials.

Cobalt sulfide (CoS), as a semiconductor metal sulfide, exhibits superior theoretical capacity and good electrical properties in the fields of supercapacitors and lithium batteries [26–29]. In recent years, CoS hybrid absorption composites have attracted much attention. Huang et al. prepared a heterostructure MWCNTs/CoS material, which consisted of numerous CoS nanoplates anchored with MWCNTs, and obtained good EM wave absorption performance [30]. Our groups fabricated cole-shell structure CoS@ppy composites, which showed an optimal RL of –41.8 dB at 6.96 GHz with a filler loading of 20 wt % [31]. In addition, Zhang et al. fabricated a CoS/MXene composite that showed outstanding electrochemical performance, and the MXene, acting like a circuit plate, provided a conductive network for CoS [32]. It has been considered to combine high conductivity $Ti_3C_2T_x$ MXene with CoS nanoparticles to synthesize absorption materials. To our knowledge, no such reports have been reported. The laminated structure of MXene can increase the EM wave propagation path, which is beneficial to enhance the attenuation of EM waves through scattering. As a result of the negative charges reaction, Co^{2+} ions can be absorbed on the surface of MXene. Moreover, the defects will act as polarization centers and induce polarization relaxation under alternating electromagnetic fields. The introduction of nanoscale particles into the material can be beneficial to increase the polarization loss and enhance the absorption of EM waves. Considering the excellent multiple structure of $Ti_3C_2T_x$ nanosheets and the greatly increased interfaces induced by the CoS composites, it is significant to explore the CoS@$Ti_3C_2T_x$ MXene hybrid for EM wave absorption.

Herein, in this study, sandwich-like CoS@$Ti_3C_2T_x$ MXene composites were successfully prepared via a solvothermal method and first used as a high-efficiency EM wave absorber. The morphology, crystalline structure, and EM absorption properties of CoS@$Ti_3C_2T_x$ MXene materials were investigated. Moreover, the attenuation mechanisms of EM waves were also illustrated such as dipole polarization, interfacial polarization, dielectric loss, and impedance matching. The results indicate that the CoS/$Ti_3C_2T_x$ MXene composites is a potential candidate for the EM wave absorbing composite, which possesses strong absorption and broad bandwidth.

2. Materials and Methods

2.1. Materials

Ti_3AlC_2 powders (purity > 99%, 200 mesh) were obtained from Changchun 11 Technology Co. Ltd. (Changchun, China). Lithium fluoride (LiF) (purity > 99%) and hydrochloric acid (HCl) (36–38%) were obtained from Macklin Technology Ltd. (Shanghai, China). Ethylene glycol (EG, AR), cobalt chloride hexahydrate ($CoCl_2 \cdot 6H_2O$, AR), and thiourea (CN_2H_4S, AR) were provided from Aladdin Technology Co. Ltd. (Shanghai, China).

2.2. Synthesis of $Ti_3C_2T_x$ MXene

$Ti_3C_2T_x$ MXene was synthesized based on the previous work [33]. First, 1 g LiF was completely dissolved in 20 mL of 9 M HCl solution with stirring for 5 min at room temperature. Then, 1 g Ti_3AlC_2 powder was slowly added into the above solution and kept stirring at 45 °C for 24 h. Subsequently, the homogeneous mixture was washed three times using deionized water by centrifuge (3500 rpm) until the pH reached 6. Finally, the obtained black samples were dried in the desiccator under vacuum at 50 °C.

2.3. Synthesis of CoS@$Ti_3C_2T_x$ Hybrids

The synthesis of CoS@$Ti_3C_2T_x$ hybrids was carried out in a solvothermal reaction. In detail, 200 mg $Ti_3C_2T_x$ MXene was dissolved in 20 mL EG by ultrasound for 1 h. Then, 2.5 mmol $CoCl_2 \cdot 6H_2O$ was dispersed in 30 mL EG and mixed with the former solution, stirring for 30 min. Subsequently, the 20 mL EG solution dissolved in 6.25 mmol thiourea was slowly added into the above solution with magnetic stirring for 30 min. The homogeneous suspension was moved into the 100 mL Teflon-lined autoclave (Shanghai Yuezhongyq Co.Ltd, Shanghai, China) and reacted at 180 °C for 12 h. Meanwhile, CoS nanoparticles were prepared for comparison. The schematic illustration of the synthesis of CoS@$Ti_3C_2T_x$ hybrids is shown in Figure 1.

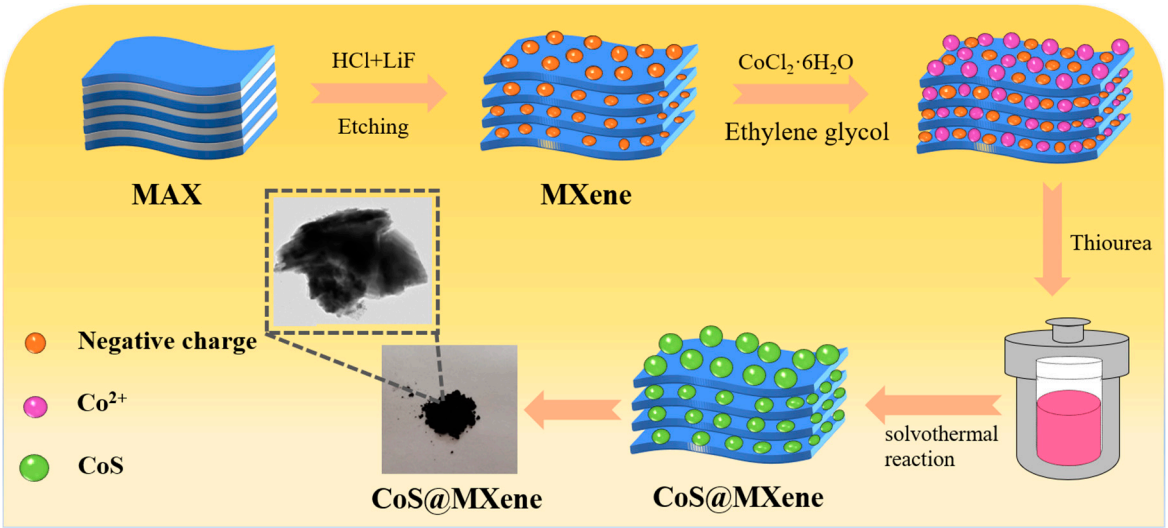

Figure 1. Schematic diagram of the synthesis of CoS@$Ti_3C_2T_x$ composites.

2.4. Characterization

The microscopic morphology of $Ti_3C_2T_x$ MXene, CoS nanoparticles, and CoS@$Ti_3C_2T_x$ composite were detected by scanning electron microscopy (SEM, JSM-7800F, JEOL, Tokyo, Japan). The microstructure and elemental mapping were characterized by an energy dispersive x-ray spectroscopy (EDS, XFlash 5030T, BRUKER, Leipzig, Germany) and a transmission electron microscope (TEM, JEM-2100F, JEOL, Tokyo, Japan) with a scanning transmission electron microscope (STEM)

resolution of 0.20 nm. X-ray diffraction (XRD, D8A Advance, BRUKER, Leipzig, Germany) was used to analyze the crystallite structure of the composites. The surface of the CoS@$Ti_3C_2T_x$ composite was performed by x-ray photoelectron spectroscopy (XPS, ESCALAB 250 xi, Shanghai, China). A vector network analyzer (VNA, N5242A PNA-X, Agilent, Palo Alto, CA, USA) was used to collect the basic EM parameters in the frequency range of 2.0–18.0 GHz at room temperature. The composite was mixed with paraffin in different filler ratios (35 wt %, 40 wt %, 45 wt %) and then pressed into a coaxial cylinder (Φ_{in} = 3.04 mm, Φ_{out} = 7.0 mm, d = 3.5 mm) under a pressure of 5 MPa.

3. Results and Discussion

3.1. Characterization of Samples

The x-ray diffraction (XRD) patterns of CoS, $Ti_3C_2T_x$, and CoS@$Ti_3C_2T_x$ are shown in Figure 2. The typical peaks at 7.2°, 17.6°, 42.0°, and 60.8° corresponded to the (002), (004), (010), and (110) crystal planes of $Ti_3C_2T_x$, respectively [34]. Obviously, the (002) peak of CoS@$Ti_3C_2T_x$ shifted to 6.1° after the solvothermal reaction. According to the Bragg equation, the layer space of $Ti_3C_2T_x$ increased from 12.2 Å to 14.4 Å, indicating the cobalt sulfide nanoparticles had anchored on the $Ti_3C_2T_x$ MXene layers to form a multilayered structure. In addition, the peaks at 30.2°, 35.14°, 46.66°, and 54.72° corresponded to the (100), (101), (102,) and (110) planes of hexagonal CoS (JCPDS No.75-0605), which indicates the successful synthesis of CoS@$Ti_3C_2T_x$ composites.

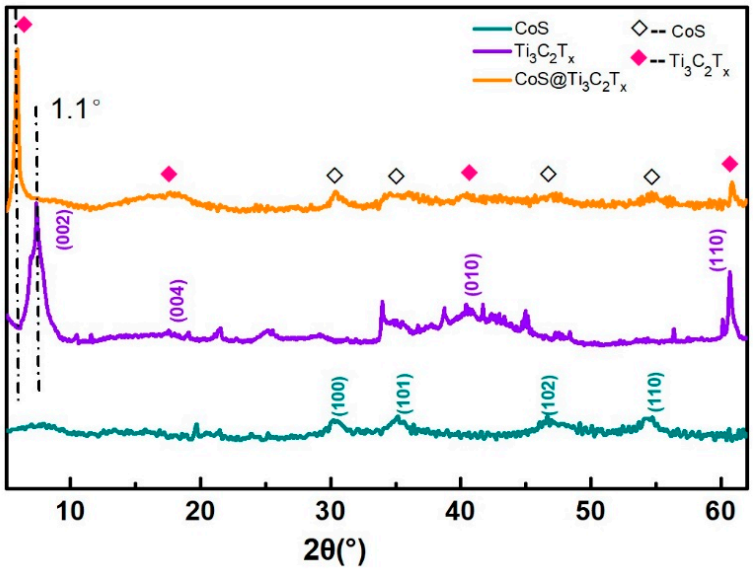

Figure 2. XRD patterns of CoS, MXene, and CoS@$Ti_3C_2T_x$.

To further research the surface chemical elements of CoS@$Ti_3C_2T_x$ composites, the XPS spectra are shown in Figure 3. As shown in Figure 3a, the total spectrum of the CoS/$Ti_3C_2T_x$ composite demonstrates the existence of Co, Ti, O, S, and C elements. Figure 3b illustrates the Ti 2p XPS spectrum of the sample and the peaks corresponding to Ti–C (454.8 eV), Ti_xC_y (457.7 eV), Ti $2p_{3/2}$ (458.3 eV), Ti–F (461.4 eV), and Ti $2p_{1/2}$ (464.1 eV) [35]. The C 1s spectra exhibited in Figure 3c contains four fitted peaks including Ti–C (281.4 eV), C–C (284.7 eV), C–O (286.3 eV), and C–F (288.7 eV) [36]. The O 1s peaks at 530.3 eV and 531.8 eV can be indexed to C–Ti–O and Ti–OH in Figure 3d [37]. Moreover, the peak at 532.8 eV confirms that there are a small number of water molecules in the $Ti_3C_2T_x$ MXene layers [38]. In Figure 3e, the peak at 793.8 eV is indexed to Co $2p_{1/2}$ and the peak located at 778.8 eV belongs to Co $2p_{3/2}$ [39]. In addition, the presence of C–S–C, C–SO_x–C, S $2p_{1/2}$, and S $2p_{3/2}$ can be observed in Figure 3f. Thus, the XPS analysis indicates that the heterogeneous structural CoS@$Ti_3C_2T_x$ composites were prepared, which also corresponded to the XRD analysis.

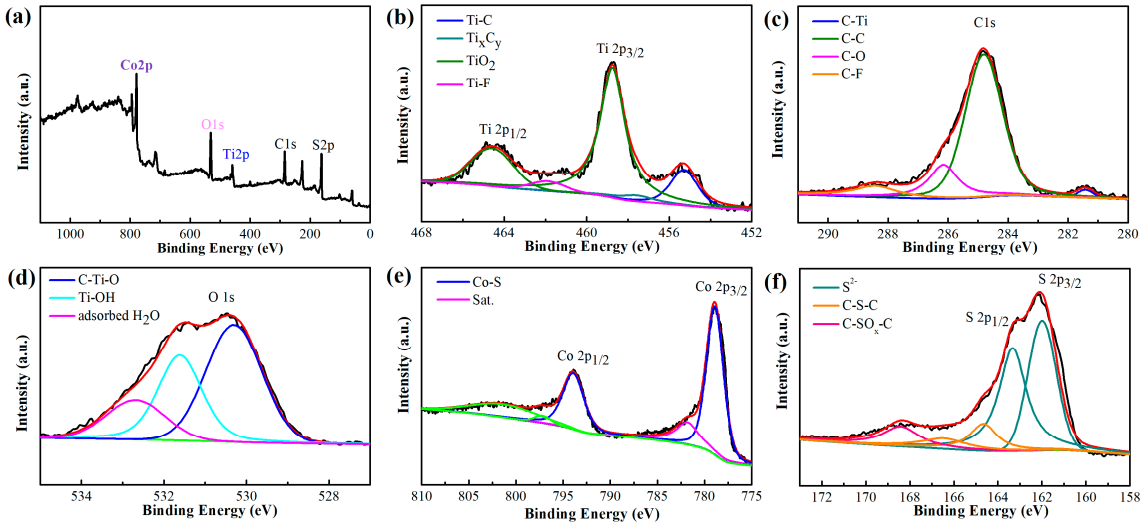

Figure 3. X-ray photoelectron spectroscopy (XPS) survey spectra of CoS@$Ti_3C_2T_x$: (**a**) survey spectrum, (**b**) Ti 2p, (**c**) C 1s, (**d**) O 1s, (**e**) Co 2p, and (**f**) S 2p.

The morphology of $Ti_3C_2T_x$ MXene is given in Figure 4a. It can be observed that $Ti_3C_2T_x$ MXene showed a similar accordion-like structure after etching. A large number of agglomerated CoS nanoparticles can be observed in Figure 4b. As shown in Figure 4c,d, CoS nanoparticles are anchored on the surface and inside the $Ti_3C_2T_x$ MXene, forming a sandwich structure. It is worth noting that the interlayer spacing of the composites is significantly larger than pure MXene. From Figure 4b, it can be found that there was obvious agglomeration of pure CoS nanoparticles. As shown in Figure 4c, when CoS nanoparticles were combined with the two-dimensional material $Ti_3C_2T_x$ MXene, Co^{2+} ions can be absorbed and dispersed by the functional groups on the surface of MXene, which effectively solved the agglomeration of CoS nanoparticles. These CoS nanoparticles will connect with $Ti_3C_2T_x$ nanosheets to form a conductive network, which may be beneficial to increase the dielectric loss of the material. Figure 5 shows the TEM of the CoS@$Ti_3C_2T_x$ composites, from which a typical laminated structure of the $Ti_3C_2T_x$ MXene can be observed. It can be seen from the elemental mapping images that the Ti, C, and O elements were uniformly distributed in the diagram. Due to the oxidation on the surface of the $Ti_3C_2T_x$ MXene, the oxygen element was detected. The distribution of Co and S further confirms the successful composition of the CoS nanoparticles and $Ti_3C_2T_x$ MXene. Moreover, the TEM image of the $Ti_3C_2T_x$ MXene in Figure 6a shows that $Ti_3C_2T_x$ MXene presents an ultrathin transparent laminated structure and the interlayer space of the $Ti_3C_2T_x$ MXene was approximately 0.99 nm, as shown in the high resolution transmission electron microscope (HRTEM) image in Figure 6b. The average diameter of CoS nanoparticles was about 15–17 nm and it can be observed that these nanoparticles were embedded in the interlayer or surface of the $Ti_3C_2T_x$ MXene nanosheets. As described in Figure 6e, the interlayer spacing of 0.25 nm and 1.03 nm corresponded to the (101) facets of the CoS nanoparticles and the (002) planes of the laminated $Ti_3C_2T_x$ MXene, respectively. In order to further demonstrate the existence of CoS nanoparticles on the surface of $Ti_3C_2T_x$ MXene, the corresponding EDS image is shown in Figure 6f. It can be seen that the five elements of Ti, Co, S, O, C were detected, and the atomic ratio of Co and S was around 1:1, which corresponds to the stoichiometry of CoS. Moreover, no other elements were found, which further confirms the successful preparation of CoS@$Ti_3C_2T_x$ composites.

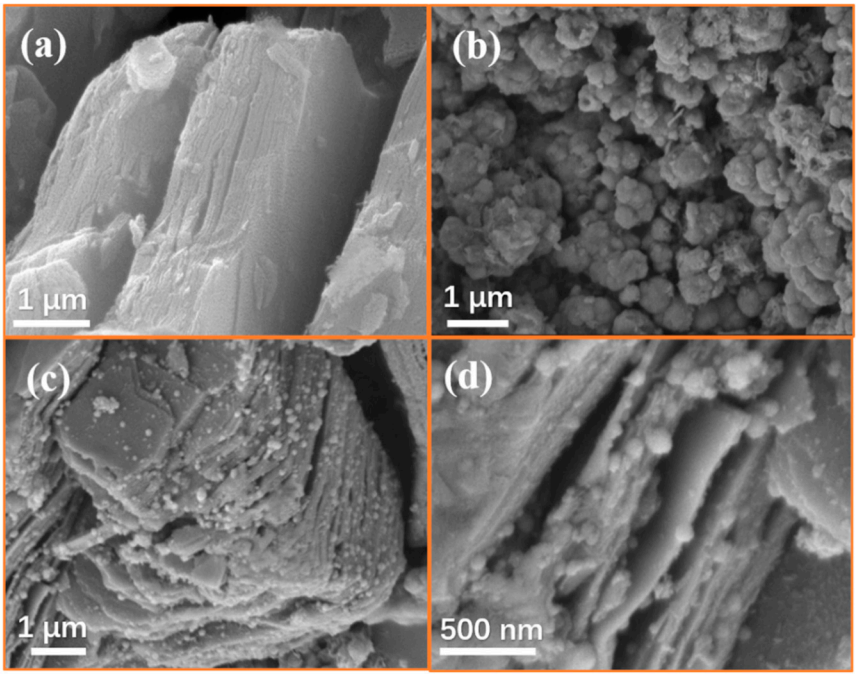

Figure 4. Scanning electron microscopy (SEM) of $Ti_3C_2T_x$ (**a**), CoS nanoparticles (**b**), CoS@$Ti_3C_2T_x$ composite (**c**,**d**).

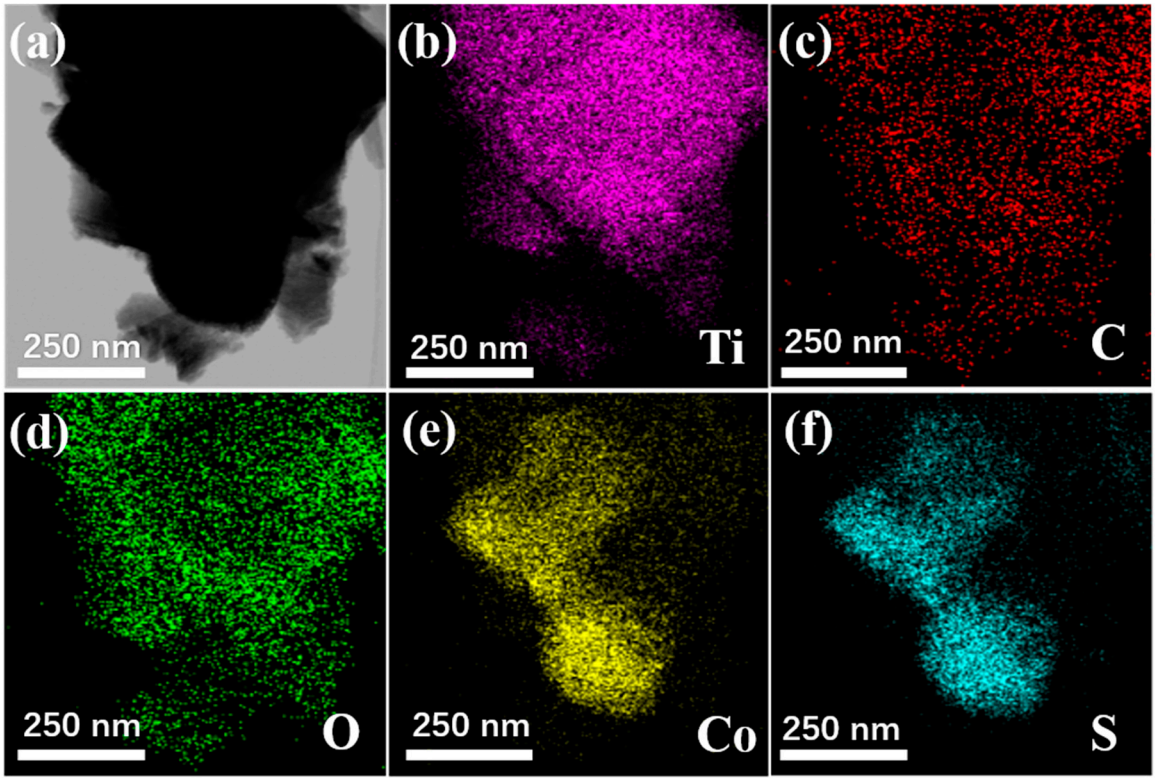

Figure 5. TEM of CoS@$Ti_3C_2T_x$ (**a**), and its corresponding elemental mapping images of Ti (**b**), C (**c**), O (**d**), Co (**e**), and S (**f**).

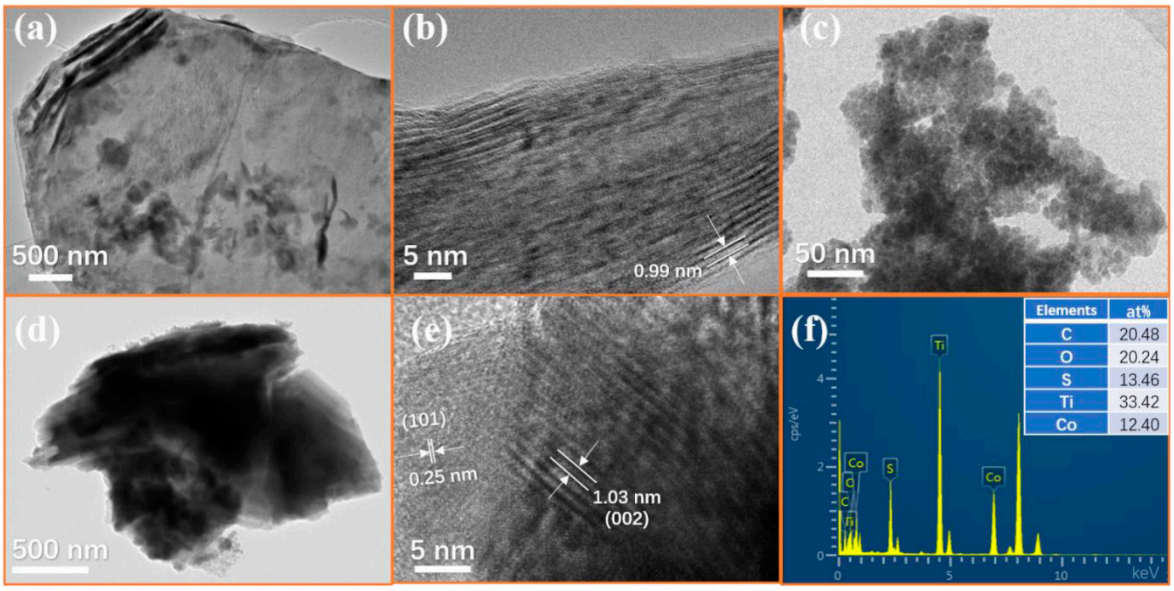

Figure 6. TEM (**a**), HRTEM (**b**) images of $Ti_3C_2T_x$, TEM image of CoS nanoparticles (**c**), TEM (**d**), HRTEM (**e**) and corresponding EDS (**f**) images of CoS@$Ti_3C_2T_x$.

3.2. Electromagnetic Parameters and Absorption Property

To evaluate the EM wave absorption characteristics, the relative complex permittivity ($\varepsilon_r = \varepsilon' - j\varepsilon''$) and relative complex permeability ($\mu_r = \mu' - j\mu''$) of the $Ti_3C_2T_x$, CoS, and CoS@$Ti_3C_2T_x$ MXene composites with different filler loading were measured using a vector network analyzer ground on the coaxial-line method in the frequency range of 2–18 GHz. The samples were mixed with paraffin and pressed into a ring model (Φ_{in} = 3.04 mm, Φ_{out} = 7.0 mm), which were then placed in a coaxial clamp. After multiple reflection and transmission between the air interface of the transmission line and the sample, the EM wave energy would attenuate and the phase would shift. Then, the scattering parameter S is measured by a vector network analyzer and the EM parameters can be calculated according to the standard Nicolson–Ross–Weir theory [40,41]. In general, the real part of the relative complex permittivity (ε') represents the polarization capability of the composite in the electric field, the real part of the relative complex permeability (μ') shows magnetization capability under the influence of a magnetic field. The imaginary part of the relative complex permittivity (ε'') and the relative complex permeability (μ'') represent dielectric loss and magnetic loss capacity, respectively [42]. As shown in Figure 7a, the average ε' and ε'' value of $Ti_3C_2T_x$ (35 wt %) were maintained at 6.9 and 0.8, respectively. In comparison, the average ε' and ε'' values of CoS (35 wt %) reached 10.0 and 2.0, respectively, as shown in Figure 7b. As the filler loading in the paraffin matrix increased from 35 wt % to 45 wt %, the ε' and ε'' values of CoS@$Ti_3C_2T_x$ added up to 13.5 and 5.1, respectively, which may be illustrated by the effective medium theory [43]. The dipole polarization, interfacial polarization, and electrical conductivity may be enhanced by the increase in CoS@$Ti_3C_2T_x$ weight [19]. As demonstrated in Figure 7d,e, it is worth noting that the ε' and ε'' curves fluctuated significantly within the 8–18 GHz, and it may be related to the relaxation polarization and interfacial polarization of dielectric materials at high frequencies. In particular, the ε' and ε'' achieved the highest values, indicating that CoS@$Ti_3C_2T_x$ (45 wt %) possibly has a favorable dielectric dissipation capability to EM waves, as shown in Figure 7e. Moreover, as shown in Figure 7, due to the absence of magnetism in these composites, the μ' and μ'' values reached 1.0 and 0, respectively. The above analysis showed that dielectric loss is the major mechanism of EM wave absorption in the CoS@$Ti_3C_2T_x$ composites, while the magnetic loss can be ignored.

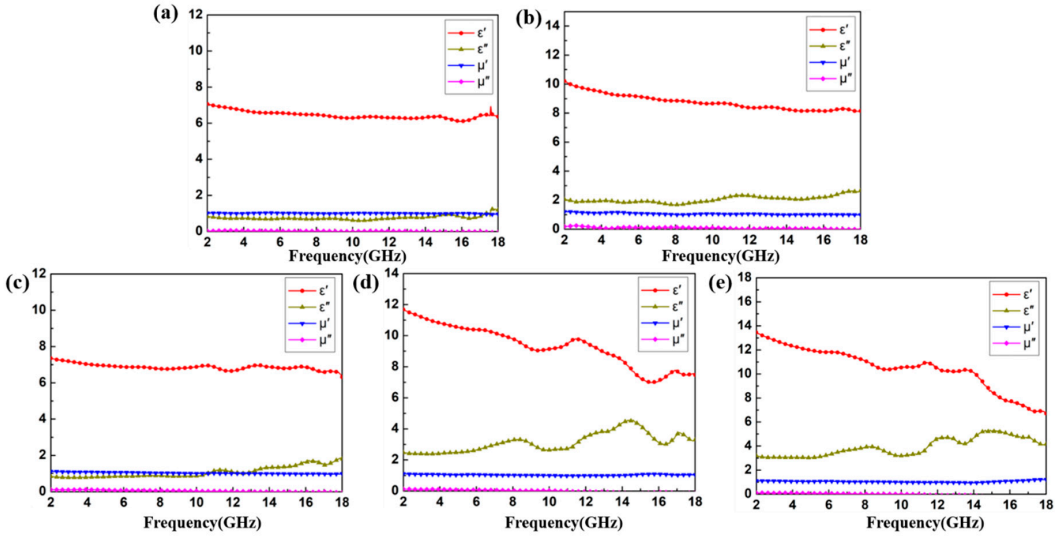

Figure 7. Real and imaginary parts of the complex permittivity and permeability of $Ti_3C_2T_x$ (35 wt %) (**a**), CoS (35 wt %) (**b**), CoS@$Ti_3C_2T_x$ (35 wt %) (**c**), CoS@$Ti_3C_2T_x$ (40 wt %) (**d**), and CoS@$Ti_3C_2T_x$ (45 wt %) (**e**).

Dielectric loss is related to two important factors: polarization relaxation and conductivity loss, and the dielectric loss tangents ($tan\ \delta_\varepsilon = \varepsilon''/\varepsilon'$) of CoS@$Ti_3C_2T_x$ composites with different filler loadings are calculated in Figure 8a. With the increase in frequency, the $\tan\delta_\varepsilon$ curves showed an upward trend and some vibration peaks corresponded well to the permittivity curves. The average values of curves at 40 wt % and 45 wt % increased from 0.25 to 0.35 at 2–10 GHz, respectively. However, as the frequency continued to increase, the value of the 45 wt % curve achieved 0.65, indicating better dielectric loss capability. A similar phenomenon can be seen in the attenuation constant (α) curves in Figure 8b, which can be calculated as follows [44]:

$$\alpha = \frac{\sqrt{2}\pi f}{c} \times \sqrt{(\mu''\varepsilon'' - \mu'\varepsilon') + \sqrt{(\mu''\varepsilon'' - \mu'\varepsilon')^2 + (\mu'\varepsilon'' + \mu''\varepsilon')^2}} \quad (1)$$

where f is frequency and c represents the velocity of light. The larger α value means a stronger EM wave dissipation ability. As shown in Figure 8b, CoS@$Ti_3C_2T_x$ (35 wt %) had a significantly lower absorption of EM waves than 40 wt % and 45 wt %. To further investigate the polarization relaxation phenomenon of CoS@$Ti_3C_2T_x$ composites, the Cole–Cole semicircle model is necessary. The Debye equation is as follows [45]:

$$\varepsilon_r = \varepsilon' + i\varepsilon'' = \varepsilon_\infty + \frac{\varepsilon_s - \varepsilon_\infty}{1 + i\omega\tau} \quad (2)$$

According to Equation (2), the ε' and ε'' can be expressed as:

$$\varepsilon' = \varepsilon_\infty + \frac{\varepsilon_s - \varepsilon_\infty}{1 + \omega^2\tau^2} \quad (3)$$

$$\varepsilon'' = \frac{\omega\tau(\varepsilon_s - \varepsilon_\infty)}{1 + \omega^2\tau^2} \quad (4)$$

where ε_s stands for the static permittivity; ε_∞ stands for the relative dielectric constant; τ is the polarization relaxation time; and ω stands for the electric field oscillation frequency. According to Equations (3) and (4), the relationship between ε' and ε'' may be described by [46]:

$$\left(\varepsilon' - \frac{\varepsilon_s + \varepsilon_\infty}{2}\right)^2 + (\varepsilon'')^2 = \left(\frac{\varepsilon_s - \varepsilon_\infty}{2}\right)^2 \quad (5)$$

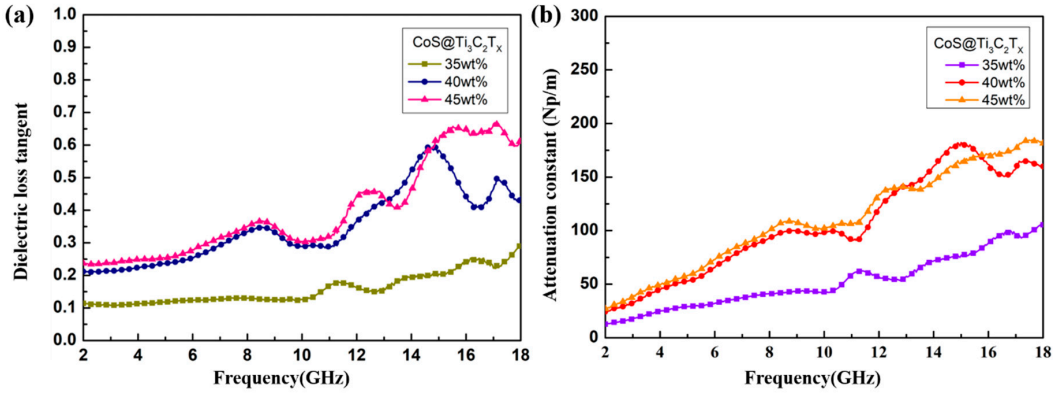

Figure 8. Dielectric loss tangent (**a**) and attenuation constant (**b**) of CoS@$Ti_3C_2T_x$ composites with different filler loadings.

The plot of ε' versus ε'' can be expressed as a Cole–Cole semicircle and each Cole–Cole semicircle corresponds to a polarization relaxation process [47]. In Figure 9a, because of the effect of the multi-relaxation dielectric properties, the Cole–Cole semicircle of $Ti_3C_2T_x$ (35 wt %) showed a complex interlacing shape. In Figure 9b, there are four small distorted semicircles in CoS (35 wt %). The reason of semicircle distortion is that the Debye equation is an ideal model built under special conditions, and there are lattice distortion and point defects in the material [48]. In Figure 9c–e, three or four distinct semicircles can be observed in the CoS@$Ti_3C_2T_x$ composites, which may result from the synergistic effects of dipole polarization and interfacial polarization [49]. More dipoles can be induced by the localized defects, oxygen functional groups, and multilayered structure of $Ti_3C_2T_x$ [17,50,51]. Furthermore, there are many CoS nanoparticles embedded on the surface of the $Ti_3C_2T_x$. According to the nanometer size effect, the number of dangling bonds, dipoles, and defects in the CoS@$Ti_3C_2T_x$ composites would increase significantly, which may obviously enhance the electronic polarization and dipole polarization [52,53]. In addition, based on the Maxwell–Wanger–Sillars (MWS) effect, the special multicomponent heterostructure might generate more interfacial polarization process and thus enhance the absorption capability of EM waves [54].

In order to further research the EM wave absorption characteristics of the CoS@$Ti_3C_2T_x$ composites, the reflection loss (RL) values versus frequency of the materials with different filler loadings at specific thickness are shown in Figure 10. As described by transmission line theory, the RL values can be calculated by [55]:

$$Z_{in} = Z_0 \sqrt{\frac{\mu_r}{\varepsilon_r}} \tanh\left[j\frac{2\pi f d}{c}\sqrt{\mu_r \varepsilon_r}\right] \quad (6)$$

$$\mathrm{RL} = 20\log\left|\frac{Z_{in} - Z_0}{Z_{in} + Z_0}\right| \quad (7)$$

where d denotes the thickness of the absorbers; and Z_{in} and Z_0 stand for the normalized input characteristic impendence and the impendence of air, respectively. Figure 10a illustrates that the maximum RL values of CoS@$Ti_3C_2T_x$ (35 wt %) at different thickness were above −10 dB, which means that the CoS@$Ti_3C_2T_x$ (35 wt %) cannot absorb EM waves effectively. Comparatively, the maximum RL value of CoS@$Ti_3C_2T_x$ (40 wt %) was −59.2 dB at 14.6 GHz and the corresponding optimal thickness was 2.0 mm, and the effective absorbing bandwidth was 5.0 GHz (12.24–17.24 GHz), as given in Figure 10b. When the filler ratio was 45 wt %, the maximum RL value of −28.83 dB at 12.32 GHz was found at a thickness of 2.0 mm, while the absorbing bandwidth below −10 dB was 4.16 GHz (11.04–15.2 GHz). After analysis, it can be found that the CoS@$Ti_3C_2T_x$ (40 wt %) composite had superior EM absorption properties. Furthermore, it is worth noting that with the increase in the absorber thickness, the maximum RL locations shifted toward lower frequencies, which is consistent with the quarter-wavelength cancellation. The simulation curve of the absorption thickness (t_m)

can be calculated by the 1/4 wavelength cancellation equation ($t_m = n\lambda/4 = nc/(4f_m\sqrt{|\mu_r||\varepsilon_r|})$) [23]. In Figure 10, the pink dots represent the matching thickness. It is interesting to observe that the pink dots were accurately distributed on the quarter-wavelength simulation curve, suggesting that the absorbing mechanism of the composite conforms to the 1/4 wavelength theory. In addition, good impedance matching is also a necessary condition for the material to have excellent absorption capability. The normalized characteristic impedance ($Z = |Z_{in}/Z_0|$) versus frequency is shown in Figure 10. Combined with the RL curves, the corresponding Z of the CoS@$Ti_3C_2T_x$ (40 wt %) was close to 1 with a thickness of 2.0 mm, indicating that the material has optimal impedance matching and good EM wave absorbing potential.

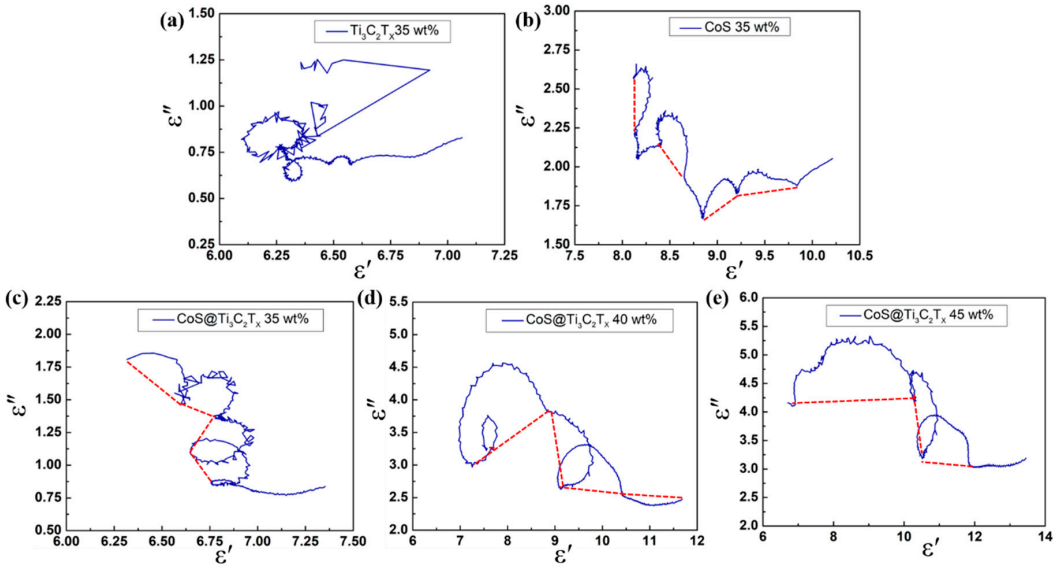

Figure 9. Typical Cole–Cole plots of $Ti_3C_2T_x$ (35 wt %) (**a**), CoS (35 wt %) (**b**), CoS@$Ti_3C_2T_x$ (35 wt %) (**c**), CoS@$Ti_3C_2T_x$ (40 wt %) (**d**), and CoS@$Ti_3C_2T_x$ (45 wt %) (**e**).

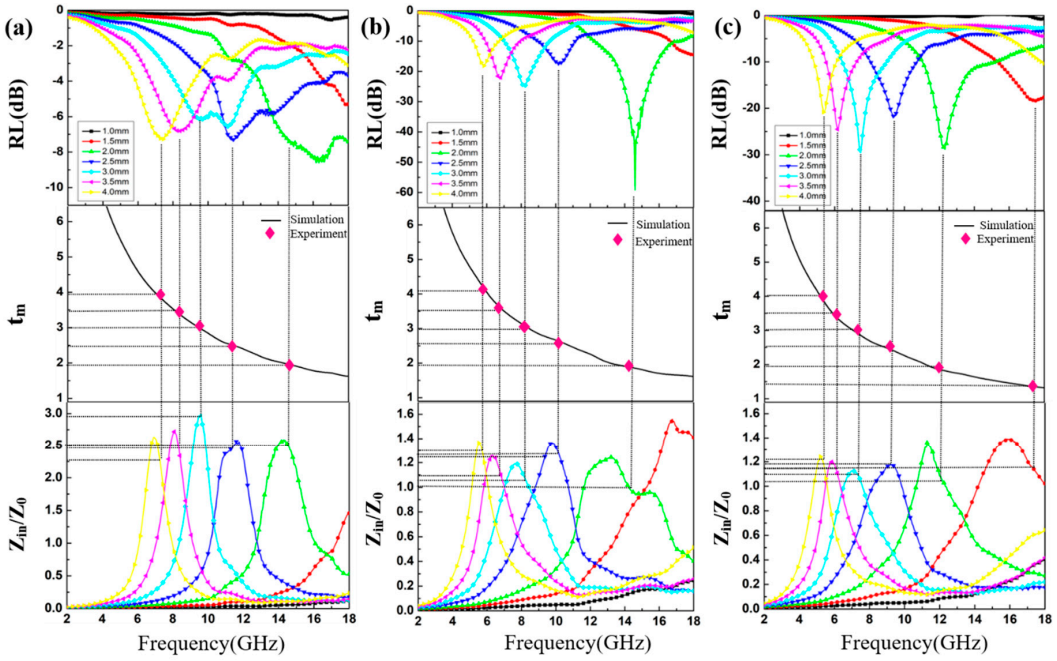

Figure 10. The RL curves, the matching thickness (t_m) under λ/4 conditions and impedance matching of CoS@$Ti_3C_2T_x$ with different filler loadings: 35 wt % (**a**), 40 wt % (**b**), and 45 wt % (**c**).

Figure 11 shows three dimensional profiles of RL values of $Ti_3C_2T_x$, CoS and CoS@$Ti_3C_2T_x$ at a 40 wt % doping ratio in the paraffin. From Figure 11a, the maximum RL value of $Ti_3C_2T_x$ was −8.24dB and cannot be used as the EM wave absorber. In Figure 11b, the CoS nanoparticles were endowed with the maximum RL value of −39.44 dB and the responding thickness was 4.0 mm at 5.2 GHz. Although the absorption strength is acceptable, the absorption thickness cannot meet the requirement of an excellent EM wave absorbing material. In Figure 11c, the CoS@$Ti_3C_2T_x$ composite exhibited the maximum RL value of −61.84 dB obtained at 14.3 GHz, and the absorbing thickness was only 1.84 mm. Moreover, when the thickness was 2.0 mm, the corresponding absorption bandwidth (RL < −10 dB) of the CoS@$Ti_3C_2T_x$ composite reached 5.0 GHz (12.24–17.24 GHz), as shown in Figure 11d. Obviously, the CoS@$Ti_3C_2T_x$ composite exhibited strong absorption intensity and broad effective bandwidth than that of the CoS and $Ti_3C_2T_x$ composite due to their limited impedance matching.

To further explain the attenuation process of EM waves in the CoS@$Ti_3C_2T_x$ composite, a schematic diagram of the proposed absorption mechanism is given in Figure 12. First, due to good impedance matching, more incident EM waves could enter the material and be absorbed rather than reflected. Second, the unique sandwich structure of the CoS@$Ti_3C_2T_x$ composite will expand the propagation path of EM waves inside the material, which may be conductive to the conversion of the EM waves into heat energy [56]. Meanwhile, based on the space-charge polarization effect, the interlayer space of the $Ti_3C_2T_x$ MXene increased because of the existence of these nanoparticles, which perhaps benefits the enhancement of the absorption capacity [57,58]. Third, the introduction of CoS nanoparticles will significantly increase the conductive paths in the $Ti_3C_2T_x$ MXene, carriers will migrate and hop between the $Ti_3C_2T_x$ layers more actively. The formed field induced microcurrent may contribute to the conduction loss [59]. Moreover, abundant surface defects, dangling bonds, and functional groups (–F, –O, –OH) in $Ti_3C_2T_x$ layers will form many polarized centers and generate a large number of dipoles, enhancing the dipolar polarization loss [60,61]. Finally, the interfacial polarization between CoS nanoparticles and $Ti_3C_2T_x$ MXene sheets also favors the attenuation of EM waves. Thus, under the comprehensive influence of these factors, the CoS@$Ti_3C_2T_x$ composite illustrates impressive absorption potential.

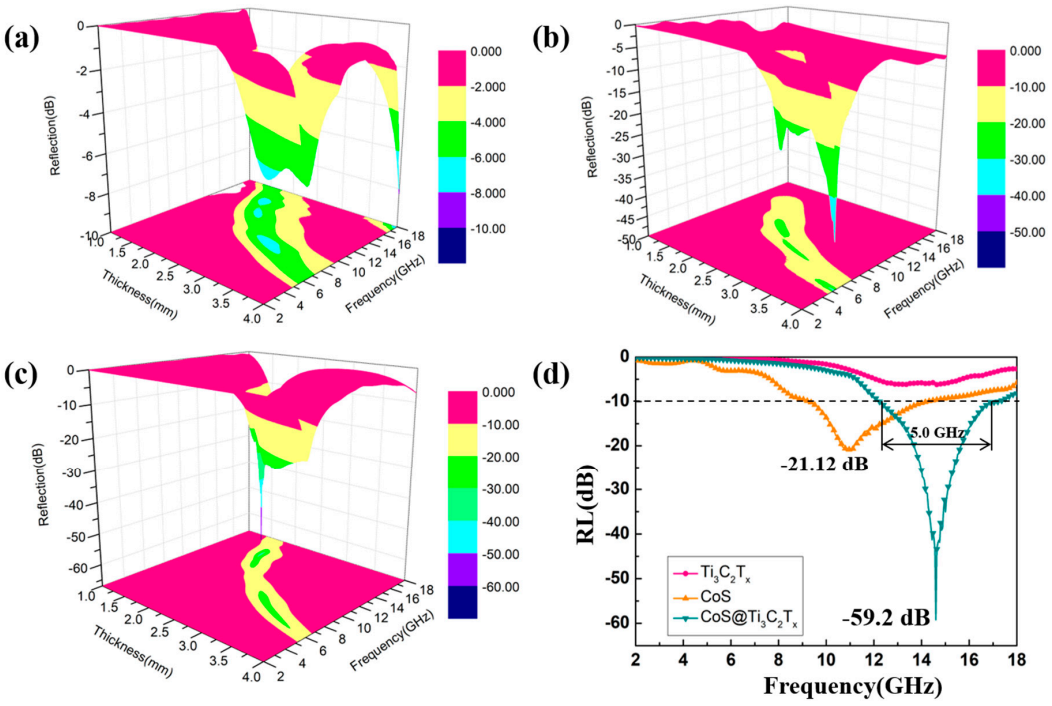

Figure 11. Three dimensional profiles of RL values of $Ti_3C_2T_x$ (40 wt %) (**a**), CoS (40 wt %) (**b**), CoS@$Ti_3C_2T_x$ (40 wt %) (**c**), and the RL curves at the thickness of 2.0 mm for them (**d**).

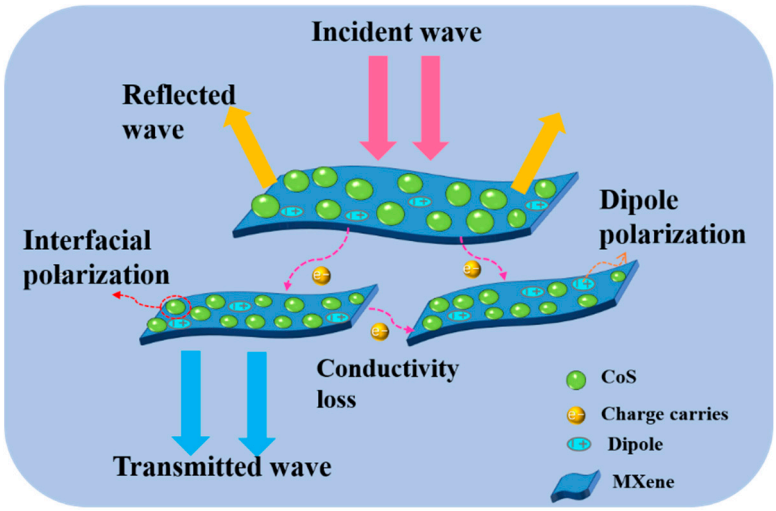

Figure 12. Scheme of EM wave absorbing mechanism of the CoS@$Ti_3C_2T_x$ composites.

4. Conclusions

In this work, a CoS@$Ti_3C_2T_x$ composite was successfully fabricated through a solvothermal reaction. After combining with $Ti_3C_2T_x$ MXene, the impedance matching of the CoS@$Ti_3C_2T_x$ composite had been significantly optimized. Enhanced dielectric loss, interfacial polarization, and unique sandwich structure also contributed to the EM wave absorption. As a result, the as prepared CoS@$Ti_3C_2T_x$ composite showed excellent EM wave absorbing properties with the maximum RL value reaching −59.2 dB at an optimal thickness of only 2.0 mm. The effective absorbing bandwidth was up to 5.0 GHz (from 12.24 to 17.24 GHz). Therefore, our work offers an effective way to broaden the application fields for the development of other MXene-based absorbers.

Author Contributions: H.L. conceived and designed the experiments; X.W., Z.Z., and X.L. performed the experiments; L.L. analyzed the data; H.L. and G.C. wrote the paper. All authors have read and agreed to the published version of the manuscript.

Funding: This paper was subsidized by the Foundation Strengthening Program Technical Field Fund (No. 2019-JCJQ-JJ-005). It was also supported by National Defense Science and Technology Key Laboratory Fund of China (No. 6142206180204) and the Equipment Research Fund (No. JX2015043106A11028).

Conflicts of Interest: The authors declare no conflict of interest.

References

1. Zhang, Y.; Huang, Y.; Zhang, T.F.; Chang, H.C.; Xiao, P.S.; Chen, H.H.; Huang, Z.Y.; Chen, Y.S. Broadband and Tunable High-Performance Microwave Absorption of an Ultralight and Highly Compressible Graphene Foam. *Adv. Mater.* **2015**, *27*, 2049–2053. [CrossRef] [PubMed]
2. Sun, G.B.; Dong, B.X.; Cao, M.H.; Wei, B.Q.; Hu, C.W. Hierarchical Dendrite-Like Magnetic Materials of Fe_3O_4, gamma-Fe_2O_3, and Fe with High Performance of Microwave Absorption. *Chem. Mater.* **2011**, *23*, 1587–1593. [CrossRef]
3. Qin, F.; Brosseau, C. A review and analysis of microwave absorption in polymer composites filled with carbonaceous particles. *J. Appl. Phys.* **2012**, *111*, 24. [CrossRef]
4. Sun, X.; He, J.P.; Li, G.X.; Tang, J.; Wang, T.; Guo, Y.X.; Xue, H.R. Laminated magnetic graphene with enhanced electromagnetic wave absorption properties. *J. Mater. Chem. C* **2013**, *1*, 765–777. [CrossRef]
5. Du, Y.C.; Liu, W.W.; Qiang, R.; Wang, Y.; Han, X.J.; Ma, J.; Xu, P. Shell Thickness-Dependent Microwave Absorption of Core-Shell Fe_3O_4@C Composites. *ACS Appl. Mater. Interfaces* **2014**, *6*, 12997–13006. [CrossRef] [PubMed]
6. Bose, S.; Kuila, T.; Uddin, M.E.; Kim, N.H.; Lau, A.K.T.; Lee, J.H. In-situ synthesis and characterization of electrically conductive polypyrrole/graphene nanocomposites. *Polymer* **2010**, *51*, 5921–5928. [CrossRef]

7. Zhang, X.J.; Wang, G.S.; Cao, W.Q.; Wei, Y.Z.; Liang, J.F.; Guo, L.; Cao, M.S. Enhanced Microwave Absorption Property of Reduced Graphene Oxide (RGO)-$MnFe_2O_4$ Nanocomposites and Polyvinylidene Fluoride. *ACS Appl. Mater. Interfaces* **2014**, *6*, 7471–7478. [CrossRef]
8. Najim, M.; Modi, G.; Mishra, Y.K.; Adelung, R.; Singh, D.; Agarwala, V. Ultra-wide bandwidth with enhanced microwave absorption of electroless Ni-P coated tetrapod-shaped ZnO nano- and microstructures. *Phys. Chem. Chem. Phys.* **2015**, *17*, 22923–22933. [CrossRef]
9. Wang, X.; Lu, Y.; Zhu, T.; Chang, S.; Wang, W. CoFe2O4/N-doped reduced graphene oxide aerogels for high-performance microwave absorption. *Chem. Eng. J.* **2020**, *388*, 124317. [CrossRef]
10. Li, X.L.; Yin, X.W.; Song, C.Q.; Han, M.K.; Xu, H.L.; Duan, W.Y.; Cheng, L.F.; Zhang, L.T. Self-Assembly Core-Shell Graphene-Bridged Hollow MXenes Spheres 3D Foam with Ultrahigh Specific EM Absorption Performance. *Adv. Funct. Mater.* **2018**, *28*, 8. [CrossRef]
11. Zhao, L.; Dong, B.L.; Li, S.Z.; Zhou, L.J.; Lai, L.F.; Wang, Z.W.; Zhao, S.L.; Han, M.; Gao, K.; Lu, M.; et al. Interdiffusion Reaction-Assisted Hybridization of Two-Dimensional Metal-Organic Frameworks and Ti_3C_2Tx Nanosheets for Electrocatalytic Oxygen Evolution. *ACS Nano* **2017**, *11*, 5800–5807. [CrossRef] [PubMed]
12. Yan, J.; Ren, C.E.; Maleski, K.; Hatter, C.B.; Anasori, B.; Urbankowski, P.; Sarycheva, A.; Gogotsi, Y. Flexible MXene/Graphene Films for Ultrafast Supercapacitors with Outstanding Volumetric Capacitance. *Adv. Funct. Mater.* **2017**, *27*, 10. [CrossRef]
13. Shahzad, F.; Alhabeb, M.; Hatter, C.B.; Anasori, B.; Hong, S.M.; Koo, C.M.; Gogotsi, Y. Electromagnetic interference shielding with 2D transition metal carbides (MXenes). *Science* **2016**, *353*, 1137–1140. [CrossRef] [PubMed]
14. Dai, B.Z.; Zhao, B.; Xie, X.; Su, T.T.; Fan, B.B.; Zhang, R.; Yang, R. Novel two-dimensional Ti_3C_2Tx MXenes/nano- carbon sphere hybrids for high-performance microwave absorption. *J. Mater. Chem. C* **2018**, *6*, 5690–5697. [CrossRef]
15. Halim, J.; Kota, S.; Lukatskaya, M.R.; Naguib, M.; Zhao, M.Q.; Moon, E.J.; Pitock, J.; Nanda, J.; May, S.J.; Gogotsi, Y.; et al. Synthesis and Characterization of 2D Molybdenum Carbide (MXene). *Adv. Funct. Mater.* **2016**, *26*, 3118–3127. [CrossRef]
16. Jiang, X.T.; Liu, S.X.; Liang, W.Y.; Luo, S.J.; He, Z.L.; Ge, Y.Q.; Wang, H.D.; Cao, R.; Zhang, F.; Wen, Q.; et al. Broadband Nonlinear Photonics in Few-Layer MXene Ti_3C_2Tx (T. = F., O., or OH). *Laser Photon. Rev.* **2018**, *12*, 10. [CrossRef]
17. Naguib, M.; Kurtoglu, M.; Presser, V.; Lu, J.; Niu, J.J.; Heon, M.; Hultman, L.; Gogotsi, Y.; Barsoum, M.W. Two-Dimensional Nanocrystals Produced by Exfoliation of Ti_3AlC_2. *Adv. Mater.* **2011**, *23*, 4248–4253. [CrossRef]
18. Sang, X.H.; Xie, Y.; Lin, M.W.; Alhabeb, M.; Van Aken, K.L.; Gogotsi, Y.; Kent, P.R.C.; Xiao, K.; Unocic, R.R. Atomic Defects in Monolayer Titanium Carbide (Ti_3C_2Tx) MXene. *ACS Nano* **2016**, *10*, 9193–9200. [CrossRef]
19. Zhang, J.Y.; Xue, W.; Chen, X.Y. Ti_3C_2Tx MXenes as thin broadband absorbers. *Nanotechnology* **2020**, *31*, 8. [CrossRef]
20. Wang, L.B.; Liu, H.; Lv, X.L.; Cui, G.Z.; Gu, G.X. Facile synthesis 3D porous MXene Ti_3C_2Tx@RGO composite aerogel with excellent dielectric loss and electromagnetic wave absorption. *J. Alloys Compd.* **2020**, *828*, 10. [CrossRef]
21. Li, N.; Xie, X.; Lu, H.X.; Fan, B.B.; Wang, X.H.; Zhao, B.; Zhang, R.; Yang, R. Novel two-dimensional Ti_3C_2Tx/Ni-spheres hybrids with enhanced microwave absorption properties. *Ceram. Int.* **2019**, *45*, 22880–22888. [CrossRef]
22. Li, X.L.; Zhu, J.F.; Wang, L.; Wu, W.L.; Fang, Y. In-situ growth of carbon nanotubes on two-dimensional titanium carbide for enhanced electrochemical performance. *Electrochim. Acta* **2017**, *258*, 291–301. [CrossRef]
23. Liu, R.; Li, W.H. High-Thermal-Stability and High-Thermal-Conductivity Ti_3C_2Tx MXene/Poly(vinyl alcohol) (PVA) Composites. *ACS Omega* **2018**, *3*, 2609–2617. [CrossRef] [PubMed]
24. Liu, P.; Yao, Z.; Ng, V.M.H.; Zhou, J.; Kong, L.B.; Yue, K. Facile synthesis of ultrasmall Fe_3O_4 nanoparticles on MXenes for high microwave absorption performance. *Compos. Part. A Appl. Sci. Manuf.* **2018**, *115*, 371–382. [CrossRef]
25. Cui, G.; Wang, L.; Li, L.; Xie, W.; Gu, G. Synthesis of CuS nanoparticles decorated Ti_3C_2Tx MXene with enhanced microwave absorption performance. *Prog. Nat. Sci. Mater. Int.* **2020**. [CrossRef]

26. Luo, Y.D.; Shen, J.; Cheng, R.; Chen, X.H.; Chen, Y.W.; Sun, Z.; Huang, S.M. Facile synthesis of mixed-phase cobalt sulfide counter electrodes for efficient dye sensitized solar cells. *J. Mater. Sci. Mater. Electron.* **2015**, *26*, 42–48. [CrossRef]
27. Gurumoorthy, G.; Rani, P.J.; Thirumaran, S.; Ciattini, S. Cobalt (III) dithiocarbamates for anion sensing and preparation of cobalt sulfide and cobalt-iron sulfide nanoparticles: Photocatalytic degradation of dyes with as-prepared nanoparticles. *Inorg. Chim. Acta* **2017**, *455*, 132–139. [CrossRef]
28. Yang, J.; Bao, C.X.; Zhu, K.; Yu, T.; Li, F.M.; Liu, J.G.; Li, Z.S.; Zou, Z.G. High catalytic activity and stability of nickel sulfide and cobalt sulfide hierarchical nanospheres on the counter electrodes for dye-sensitized solar cells. *Chem. Commun.* **2014**, *50*, 4824–4826. [CrossRef]
29. Li, L.L.; Ding, Y.H.; Huang, H.J.; Yu, D.S.; Zhang, S.Y.; Chen, H.Y.; Ramakrishna, S.; Peng, S.J. Controlled synthesis of unique Co_9S_8 nanostructures with carbon coating as advanced electrode for solid-state asymmetric supercapacitors. *J. Colloid Interface Sci.* **2019**, *540*, 389–397. [CrossRef]
30. Huang, T.Y.; He, M.; Zhou, Y.M.; Pan, W.L.; Li, S.W.; Ding, B.B.; Huang, S.; Tong, Y. Fabrication and microwave absorption of multiwalled carbon nanotubes anchored with CoS nanoplates. *J. Mater. Sci. Mater. Electron.* **2017**, *28*, 7622–7632. [CrossRef]
31. Liu, H.; Cui, G.Z.; Li, L.; Zhang, Z.; Lv, X.L.; Wang, X.X. Polypyrrole Chains Decorated on CoS Spheres: A Core-Shell Like Heterostructure for High-Performance Microwave Absorption. *Nanomaterials* **2020**, *10*, 166. [CrossRef] [PubMed]
32. Zhang, Y.; Zhan, R.; Xu, Q.; Liu, H.; Tao, M.; Luo, Y.; Bao, S.; Li, C.; Xu, M. Circuit board-like CoS/MXene composite with superior performance for sodium storage. *Chem. Eng. J.* **2019**, *357*, 220–225. [CrossRef]
33. Sun, R.H.; Zhang, H.B.; Liu, J.; Xie, X.; Yang, R.; Li, Y.; Hong, S.; Yu, Z.Z. Highly Conductive Transition Metal Carbide/Carbonitride(MXene) polystyrene Nanocomposites Fabricated by Electrostatic Assembly for Highly Efficient Electromagnetic Interference Shielding. *Adv. Funct. Mater.* **2017**, *27*, 11. [CrossRef]
34. Ghidiu, M.; Halim, J.; Kota, S.; Bish, D.; Gogotsi, Y.; Barsourm, M.W. Ion-Exchange and Cation Solvation Reactions in Ti_3C_2 MXene. *Chem. Mater.* **2016**, *28*, 3507–3514. [CrossRef]
35. Han, M.K.; Yin, X.W.; Li, X.L.; Anasori, B.; Zhang, L.T.; Cheng, L.F.; Gogotsi, Y. Laminated and Two-Dimensional Carbon-Supported Microwave Absorbers Derived from MXenes. *ACS Appl. Mater. Interfaces* **2017**, *9*, 20038–20045. [CrossRef]
36. Wilhelmsson, O.; Palmquist, J.P.; Lewin, E.; Emmerlich, J.; Eklund, P.; Persson, P.O.A.; Hogberg, H.; Li, S.; Ahuja, R.; Eriksson, O.; et al. Deposition and characterization of ternary thin films within the Ti-Al-C system by DC magnetron sputtering. *J. Cryst. Growth* **2006**, *291*, 290–300. [CrossRef]
37. Dang, B.H.Q.; Rahman, M.; MacElroy, D.; Dowling, D.P. Evaluation of microwave plasma oxidation treatments for the fabrication of photoactive un-doped and carbon-doped TiO_2 coatings. *Surf. Coat. Technol.* **2012**, *206*, 4113–4118. [CrossRef]
38. Fan, B.; Li, N.; Dai, B.; Shang, S.; Guan, L.; Zhao, B.; Wang, X.; Bai, Z.; Zhang, R. Investigation of adjacent spacing dependent microwave absorption properties of lamellar structural Ti_3C_2Tx MXenes. *Adv. Powder Technol.* **2020**, *31*, 808–815. [CrossRef]
39. Miao, X.H.; Pan, K.; Wang, G.F.; Liao, Y.P.; Wang, L.; Zhou, W.; Jiang, B.J.; Pan, Q.J.; Tian, G.H. Well-Dispersed CoS Nanoparticles on a Functionalized Graphene Nanosheet Surface: A Counter Electrode of Dye-Sensitized Solar Cells. *Chem. Eur. J.* **2014**, *20*, 474–482. [CrossRef]
40. Li, Z.X.; Li, X.H.; Zong, Y.; Tan, G.G.; Sun, Y.; Lan, Y.Y.; He, M.; Ren, Z.Y.; Zheng, X.L. Solvothermal synthesis of nitrogen-doped graphene decorated by superparamagnetic Fe_3O_4 nanoparticles and their applications as enhanced synergistic microwave absorbers. *Carbon* **2017**, *115*, 493–502. [CrossRef]
41. Nicolson, A.M.; Ross, G.F. Measurement of the intrinsic properties of materials by time-domain techniques. *IEEE Trans. Instrum. Meas.* **1970**, *19*, 377–382. [CrossRef]
42. Wu, H.J.; Qu, S.H.; Lin, K.J.; Qing, Y.C.; Wang, L.D.; Fan, Y.C.; Fu, Q.H.; Zhang, F.L. Enhanced low-frequency microwave absorbing property of SCFs@TiO_2 composite. *Powder Technol.* **2018**, *333*, 153–159. [CrossRef]
43. Weissker, H.C.; Furthmuller, J.; Bechstedt, F. Validity of effective-medium theory for optical properties of embedded nanocrystallites from ab initio supercell calculations. *Phys. Rev. B* **2003**, *67*, 5. [CrossRef]
44. Lu, B.; Huang, H.; Dong, X.L.; Zhang, X.F.; Lei, J.P.; Sun, J.P.; Dong, C. Influence of alloy components on electromagnetic characteristics of core/shell-type Fe-Ni nanoparticles. *J. Appl. Phys.* **2008**, *104*, 6. [CrossRef]

45. Wu, T.; Liu, Y.; Zeng, X.; Cui, T.T.; Zhao, Y.T.; Li, Y.N.; Tong, G.X. Facile Hydrothermal Synthesis of Fe_3O_4/C Core-Shell Nanorings for Efficient Low-Frequency Microwave Absorption. *ACS Appl. Mater. Interfaces* **2016**, *8*, 7370–7380. [CrossRef] [PubMed]
46. Kong, L.; Yin, X.W.; Yuan, X.Y.; Zhang, Y.J.; Liu, X.M.; Cheng, L.F.; Zhang, L.T. Electromagnetic wave absorption properties of graphene modified with carbon nanotube/poly(dimethyl siloxane) composites. *Carbon* **2014**, *73*, 185–193. [CrossRef]
47. Yu, L.; Yu, L.; Dong, Y.; Zhu, Y.; Fu, Y.; Ni, Q. Compressible polypyrrole aerogel as a lightweight and wideband electromagnetic microwave absorber. *J. Mater. Sci. Mater. Electron.* **2019**, *30*, 5598–5608. [CrossRef]
48. Wang, P.; Cheng, L.F.; Zhang, Y.N.; Zhang, L.T. Synthesis of SiC nanofibers with superior electromagnetic wave absorption performance by electrospinning. *J. Alloys Compd.* **2017**, *716*, 306–320. [CrossRef]
49. Liu, J.; Cao, W.Q.; Jin, H.B.; Yuan, J.; Zhang, D.Q.; Cao, M.S. Enhanced permittivity and multi-region microwave absorption of nanoneedle-like ZnO in the X-band at elevated temperature. *J. Mater. Chem. C* **2015**, *3*, 4670–4677. [CrossRef]
50. Coleman, J.N.; Lotya, M.; O'Neill, A.; Bergin, S.D.; King, P.J.; Khan, U.; Young, K.; Gaucher, A.; De, S.; Smith, R.J.; et al. Two-Dimensional Nanosheets Produced by Liquid Exfoliation of Layered Materials. *Science* **2011**, *331*, 568–571. [CrossRef]
51. Naguib, M.; Mochalin, V.N.; Barsoum, M.W.; Gogotsi, Y. 25th Anniversary Article: MXenes: A New Family of Two-Dimensional Materials. *Adv. Mater.* **2014**, *26*, 992–1005. [CrossRef] [PubMed]
52. Xiang, J.; Li, J.L.; Zhang, X.H.; Ye, Q.; Xu, J.H.; Shen, X.Q. Magnetic carbon nanofibers containing uniformly dispersed Fe/Co/Ni nanoparticles as stable and high-performance electromagnetic wave absorbers. *J. Mater. Chem. A* **2014**, *2*, 16905–16914. [CrossRef]
53. Che, R.C.; Peng, L.M.; Duan, X.F.; Chen, Q.; Liang, X.L. Microwave absorption enhancement and complex permittivity and permeability of Fe encapsulated within carbon nanotubes. *Adv. Mater.* **2004**, *16*, 401. [CrossRef]
54. Ren, Y.L.; Wu, H.Y.; Lu, M.M.; Chen, Y.J.; Zhu, C.L.; Gao, P.; Cao, M.S.; Li, C.Y.; Ouyang, Q.Y. Quaternary Nanocomposites Consisting of Graphene, Fe_3O_4@Fe Core@Shell, and ZnO Nanoparticles: Synthesis and Excellent Electromagnetic Absorption Properties. *ACS Appl. Mater. Interfaces* **2012**, *4*, 6436–6442. [CrossRef] [PubMed]
55. Zhang, X.; Zhu, W.; Zhang, W.; Zheng, S.; Qi, S. Preparation of TiO_2/Fe_3O_4/CF composites for enhanced microwave absorbing performance. *J. Mater. Sci. Mater. Electron.* **2018**, *29*, 7194–7202. [CrossRef]
56. He, P.; Cao, M.S.; Shu, J.C.; Cai, Y.Z.; Wang, X.X.; Zhao, Q.L.; Yuan, J. Atomic Layer Tailoring Titanium Carbide MXene To Tune Transport and Polarization for Utilization of Electromagnetic Energy beyond Solar and Chemical Energy. *ACS Appl. Mater. Interfaces* **2019**, *11*, 12535–12543. [CrossRef]
57. Hong, C.S.; Chu, S.Y.; Tsai, C.C.; Su, W.C. Manganese effect on the relaxation behaviors of the space charge polarization in Pb $(Fe_{2/3}W_{1/3})_{(0.9)}$ $Ti_{0.1}O_3$ ceramics. *Ceram. Int.* **2011**, *37*, 3405–3411. [CrossRef]
58. Okatan, M.B.; Mantese, J.V.; Alpay, S.P. Effect of space charge on the polarization hysteresis characteristics of monolithic and compositionally graded ferroelectrics. *Acta Mater.* **2010**, *58*, 39–48. [CrossRef]
59. Cao, M.S.; Song, W.L.; Hou, Z.L.; Wen, B.; Yuan, J. The effects of temperature and frequency on the dielectric properties, electromagnetic interference shielding and microwave-absorption of short carbon fiber/silica composites. *Carbon* **2010**, *48*, 788–796. [CrossRef]
60. Han, M.K.; Yin, X.W.; Wu, H.; Hou, Z.X.; Song, C.Q.; Li, X.L.; Zhang, L.T.; Cheng, L.F. Ti_3C_2 MXenes with Modified Surface for High-Performance Electromagnetic Absorption and Shielding in the X-Band. *ACS Appl. Mater. Interfaces* **2016**, *8*, 21011–21019. [CrossRef]
61. Khazaei, M.; Arai, M.; Sasaki, T.; Chung, C.Y.; Venkataramanan, N.S.; Estili, M.; Sakka, Y.; Kawazoe, Y. Novel Electronic and Magnetic Properties of Two-Dimensional Transition Metal Carbides and Nitrides. *Adv. Funct. Mater.* **2013**, *23*, 2185–2192. [CrossRef]